Analysis Model for Hybrid Magnetic Energy Harvesters

Daniel Monagle, *Graduate Student Member, IEEE*, and Steven B. Leeb, *Fellow, IEEE*

***Abstract*—Current transformer magnetic energy harvesters (CTMEHs) harvest energy from the magnetic fields surrounding electrical conductors to power sensors in a battery-free manner. Detailed, nonlinear analytical power harvest models for traditional CTMEHs have been presented and validated, such that designers can quickly predict and evaluate CTMEH performance without the need for intensive finite-element simulations. No existing power harvest model, however, has been presented for "hybrid" CTMEHs, which are composed of multiple concentric transformer cores of different materials. This article presents and validates a power harvest model for hybrid, multicore CTMEHs. Our proposed model is validated at a variety of primary current excitations for multiple, nanocrystalline/silicon steel hybrid harvesters, each with inhomogeneous cross sectional areas. The model agrees with experimental data throughout the unsaturated, soft saturated, and hard saturated operating regimes. This power harvest model is a tool to accurately predict the performance of hybrid CTMEHs, expediting the harvester design process and allowing for optimization of design parameters accordingly.**

***Index Terms*—Current transformer (CT), energy harvesting, hybrid core, magnetic core, nonlinear modeling, saturation.**

I. INTRODUCTION

PREDICTIVE maintenance prevents equipment downtime by flagging and diagnosing operational wear or anomolies before they become critical failures. Condition-monitoring sensors collect the physical data, such as vibration patterns of a motor that predictive maintenance models interpret to monitor machine health. Traditional sensors, however, are battery-powered. Consequently, a massive network of condition-monitoring sensors demands an inconvenient, impractical battery replacement process for each end node in the network. An alternative solution to powering sensor networks is energy harvesting. Sensor nodes can forgo a battery supply if the system is designed to scavenge energy from its installation environment to power itself. Such energy harvesting enables a new class of battery-free sensors that power themselves intermittently and thus require little to no intervention after installation.

Existing literature has studied a multitude of harvester types. For example, solar [1], wind [2], vibration [3], and thermoelectric [4] transducers, coupled with their associated power management circuitry, have been demonstrated for mobile device, Internet of Things, and sensing applications. Even within each harvester class, the specific transducer implementation often varies. In vibrational harvesters, for example, existing solutions include cantilever beams based on piezoelectrics [5], permanent magnets [6], and combinations of the two [7]. Furthermore, some recent works have developed "hybrid" energy harvesting systems that have the capability to harvest from multiple different ambient energy sources [8], [9], [10]. Each desired sensor installation site (e.g., wilderness versus factory) naturally lends itself to a specific subset of energy harvester types based on the abundance of particular forms of available energy (e.g., solar versus magnetic fields).

Current transformer magnetic energy harvesters (CTMEHs) harvest energy from the magnetic fields around ac transmission lines and are therefore especially apt for industrial settings. CTMEHs typically exhibit relatively high power harvest densities and are not subject to the same environmental variability dependence exhibited by solar or wind harvesters. Just like the installation of a standard current transformer (CT) used for ac current measurement, a CTMEH consists of a "secondary" winding wrapped around a magnetic core that is clamped around one or a few turns of ac current-carrying conductor (the "primary" wire). The time-varying magnetic flux passing through the core induces voltage at the CTMEH secondary winding. The key difference between the standard measurement CT and a CTMEH is that the energy transferred to the secondary winding is primarily used for supplying power to low-power electronics and sensors in CTMEH applications. About ten years ago, Moon and Leeb [11] revealed the unintuitive result that allowing the CTMEH harvester core to saturate yields maximum power harvest [11]. While saturation is often avoided in other magnetics design applications, proper modeling and control of saturation is desirable and necessary for high-performing CTMEH design. Moon and Leeb [11] presented a nonlinear power harvest model to capture core saturation behavior and enable refined design of this nonlinear energy harvester. Recently, we presented a generalized analytical CTMEH power harvest model, which did not rely on the assumption that the harvester core had an extremely high permeability [12]. Other power harvest models for "single core" harvester designs include [13], [14], [15].

Received 11 September 2025; revised 11 November 2025; accepted 5 December 2025. Date of publication 10 December 2025; date of current version 25 February 2026. This work was supported in part by the Office of Naval Research Structural Acoustics Program and The Electric Ship Research and Development Consortium, and in part by the Government of Portugal through the Portuguese Foundation for International Cooperation in Science, Technology and Higher Education and was undertaken in the MIT Portugal Program. Recommended for publication by Associate Editor D. Qiu. *(Corresponding author: Daniel Monagle.)*

The authors are with the Department of Electrical Engineering and Computer Science, Massachusetts Institute of Technology, Cambridge, MA 02139 USA (e-mail: monagled@mit.edu; sbleeb@mit.edu).

Color versions of one or more figures in this article are available at https://doi.org/10.1109/TPEL.2025.3642748.

Digital Object Identifier 10.1109/TPEL.2025.3642748

In addition to modeling harvester physics, augmenting a CTMEH with additional hardware and control for enhancing energy harvest has also been of great interest in the literature. Dynamic manipulation and timing of the CTMEH core saturation significantly increased average power harvest at high voltage load levels on the core secondary [16]. Desaturation strategies using active switches and reverse biasing for enabling multiple harvester power transfer windows per half cycle of primary current have also been demonstrated [17], [18]. Alternatively, other works have presented control windings for manipulating or desaturating the core flux level [19], [20], [21]. Passive techniques using a series capacitor for shaping the core flux [16] or a parallel capacitor to resonate with the core magnetizing inductance [22] have also been shown to increase power harvest.

This article is primarily focused on the physical modeling and demonstration of a novel, “hybrid” CTMEH design that is constructed from multiple different magnetic materials. In the broader energy harvester literature, “hybrid” is often used to describe harvesting systems comprised of multiple different energy harvesting transducers (e.g., solar and radio frequency). In this article, we use “hybrid” specifically within a CTMEH context to refer to a magnetic energy harvester that is built from multiple different core materials. Some unconventional core designs and geometries have been previously explored in the literature. Gao et al. [23] proposed and validated a nonlinear power harvest model for a cascaded core structure of an easily installed split core followed by a high-permeability ungapped core. A series-connected multicore system, employing a harvester core and current sensing core, was demonstrated in [24]. A comparative study of several single core and multicore harvester designs was presented in [25]. Wang et al. [25] focused on startup performance and evaluating the “working range” of primary currents over which each core topology could operate without entering undesirable, hard saturation. A split, multimaterial, dual-core design was presented in [26], where 3-D finite element simulations were run to explore the effect of different air gap geometries on the secondary winding induced voltage. The authors in [25] and [26] introduced dual-core CTMEHs with the intention of leveraging high saturation flux density and high permeability magnetic materials in the same harvester design. No existing work has proposed, derived, and validated a nonlinear average power harvest model for a hybrid, multicore harvester.

This article presents detailed mathematical modeling and validation of multicore, hybrid CTMEHs that are constructed from concentric split toroids of different magnetic materials. We have recently demonstrated a hybrid CTMEH in direct comparison to traditional, single core nanocrystalline and single core silicon steel (si-steel) CTMEHs [27]. Our recent work validated nonlinear hybrid core flux models in SPICE under resistive loading conditions on the secondary winding, but no mathematical average power harvest expressions were derived or validated [27]. This article presents the mathematical framework for modeling the power harvest of a saturating, hybrid CTMEH. Fig. 1 shows an illustration of a generic, n-material hybrid harvester. The hybrid harvesters consists of n concentric toroidal cores. The secondary winding of the hybrid harvester is wound from the innermost radius r_0 of the innermost core material to the outermost radius r_n of the outermost core material. As shown in Fig. 2, this yields an inhomogeneous harvester cross sectional area encompassed by each secondary turn. Thus, the flux linkage of a winding in a hybrid CTMEH changes dramatically along the radial ($\hat{r}$) axis due to the diverse material composition within the cross section.

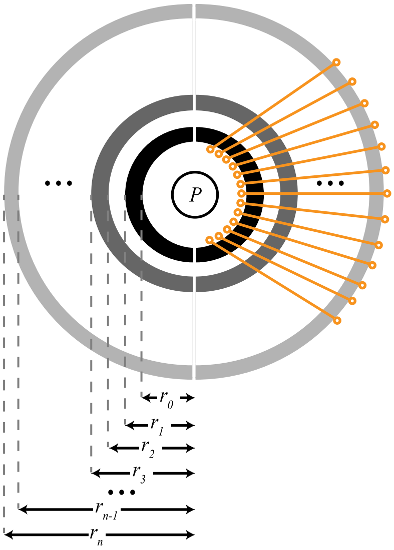

Fig. 1. Illustration of n-material, split core hybrid harvester, where different shades of gray denote different core materials.

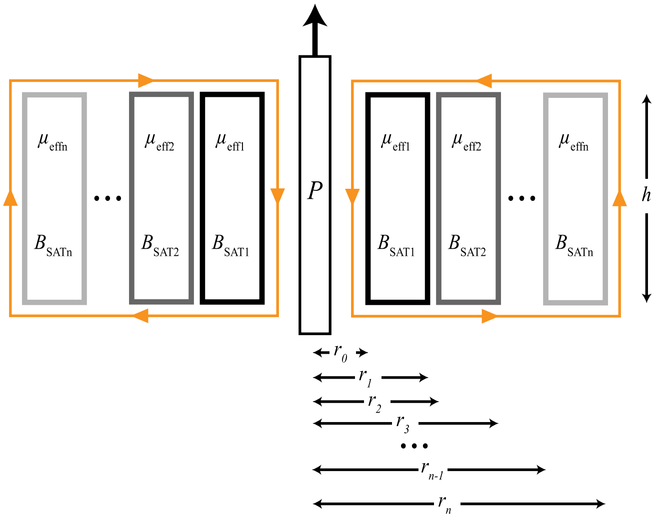

Fig. 2. Cross section of n-material hybrid harvester.

The fundamental value of the hybrid CTMEH is its ability to effectively harvest power over a very wide range of primary currents. Conversely, single material CTMEHs, generally perform well only in limited primary current ranges according to the magnetic material properties of the single harvester core. Effective initial relative permeability μ_{eff} and saturation flux density B_{SAT} are the two vital magnetic material properties that dictate the performance of the CTMEH. Higher μ_{eff} materials

TABLE I
SIMULATED POWER HARVESTS OF COMPETING CTMEH DESIGNS

I_P [$\mathrm{A_{rms}}$]	P_{MAX} [mW]			
	Nanocrystalline	Hybrid H1	Hybrid H2	Si-Steel
1.0 $\mathrm{A_{rms}}$	11.841	8.6917	9.5767	6.4723
7.5 $\mathrm{A_{rms}}$	268.64	280.04	248.66	267.25
10.0 $\mathrm{A_{rms}}$	387.64	413.25	375.93	420.75
100.0 $\mathrm{A_{rms}}$	5311.5	6700.2	6474.7	7957.4

promote strong coupling between the primary and secondary windings, while B_{SAT} sets a ceiling on the total flux that can be effectively transferred through the CTMEH core before it becomes hard saturated. Considering practical, commercially available cores, however presents a design tradeoff. State-of-the-art CTMEHs often use either nanocrystalline or si-steel cores. On one hand, nanocrystalline alloys can have effective initial relative permeabilities in excess of 100 000, much greater than that of si-steel; on the other hand, si-steel has a typical $B_{\mathrm{SAT}} \approx 2.0$T that is nearly double the typical $B_{\mathrm{SAT}} \approx 1.2$T of nanocrystalline cores. As a result, nanocrystalline cores outperform otherwise equivalent si-steel cores at "low" primary currents, which demand very high permeability to promote strong coupling and better harvesting. Under such conditions, the excess headroom of B_{SAT} provided by a si-steel harvester is underutilized. At "high" primary currents, the magnetic fields are so great that coupling is not a critical issue, and the higher B_{SAT} of a si-steel harvester causes it to harvest significantly more power than an otherwise equivalent nanocrystalline core. Consistent with the above-mentioned logic, a hybrid harvester consisting of both nanocrystalline and si-steel, can leverage its high μ_{eff} at low currents and its high B_{SAT} at high currents to yield strong power harvests over a wide range of primary currents.

To emphasize the fundamental value of hybrid cores, four illustrative, three-material CTMEHs of identical geometry, but different materials, were simulated with the power harvest model that we will propose and validate in Sections III and V of this article. The model assumes a dc voltage load connected to the secondary winding of the CTMEH through a full bridge rectifier. Each hybrid CTMEH design consisted of an inner split core, an outer split core, and a small air region between the inner and outer cores. Two of the CTMEHs were simulated where the inner and outer split cores were the same material: either only nanocrystalline or only si-steel. The other two CTMEHs were hybrid designs, where hybrid "H1" refers to the design with an inner si-steel core and an outer nanocrystalline core, and "H2" has the opposite ordering, with an inner nanocrystalline core and an outer si-steel core. For different 60 Hz sinusoidal primary current (I_P) operating conditions, the dc voltage load on the CTMEH secondary was swept in simulation to find each harvester's maximum average power harvest P_{MAX} at each I_P. The simulated P_{MAX} values are recorded in Table I.At each primary current, the greatest P_{MAX} among all the designs is highlighted green. Red highlighting denotes the smallest P_{MAX} at each I_P, unless that "worst" P_{MAX} among the designs is $\geq 70\%$ of the best power harvest. When the worst P_{MAX} is $\geq 70\%$ of the best harvest, the cell is shaded orange. Otherwise, the power harvest is highlighted yellow, indicating that it is not associated with the best or worst performing CTMEH design, but that it is still $\geq 70\%$ of the best-performing design at that current. The simulation results emphasize that a hybrid design maintains a competitive power harvest at "low," "medium," and "high" currents while the nanocrystalline and si-steel thrive or suffer depending on the primary current regime. That is the key value proposition of the hybrid core. This summarizing table introduces some intuition about the utility gained from a hybrid core, but a formal derivation of hybrid CTMEH saturation characteristics and power harvest is necessary to catalyze further exploration and design of these systems.

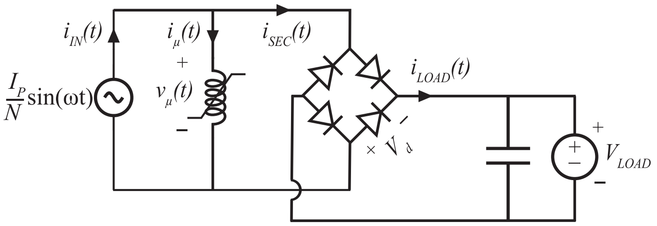

Fig. 3. Lossless CTMEH circuit model with full bridge rectifier and constant dc voltage load on the secondary winding.

The key contribution of this work is the derivation and validation of a nonlinear power harvest model for saturable, hybrid CTMEHs. We aim for the model presented in this work to enable designers to investigate hybrid cores of a variety of material compositions and arrangements. The rest of this article is structured as follows. In Section II, some background on the CTMEH circuit model and its typical voltage and current waveforms is presented. Certain relevant features of the CTMEH circuit are highlighted, as they will be critical to the detailed nonlinear power harvest derivation. Next, in Section III, we derive our average power harvest model for a saturating, multicore hybrid CTMEH. Section IV elaborates on model augmentations to capture the effects of parasitic elements, such as core loss, on power harvest. Section V presents the experimental setup and validates our power harvest model against two, different, experimental hybrid cores. Section VI then discusses implications for hybrid CTMEH designs. Finally, Section VII concludes this article.

II. CTMEH BACKGROUND

This section serves to summarize some general key features of CTMEHs that are leveraged in the derivation of our power harvest model as follows. A lossless circuit model of a general CTMEH is shown in Fig. 3, where the secondary winding of the CTMEH is connected to a constant dc voltage load through a full bridge rectifier. This dc voltage load is representative of, for example, a capacitive buffer at the input voltage rail of a dc–dc converter for a sensor package, which is a practical use-case for a CTMEH. Furthermore, recent literature has demonstrated that CTMEHs exhibit maximum power harvest operating points that are less sensitive to primary current variations when the secondary is dc voltage loaded rather than resistively loaded [28]. Our previous work has validated a SPICE model for the hybrid CTMEH under resistive loading conditions [27]. The SPICE model can be a useful tool for exploring the effects of

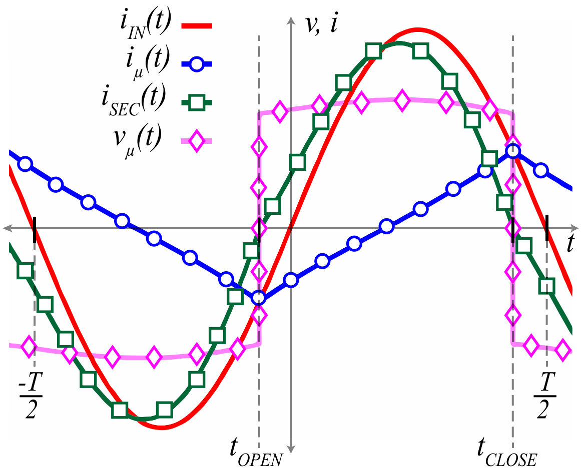

Fig. 4. Typical CTMEH circuit waveforms in **unsaturated** operation.

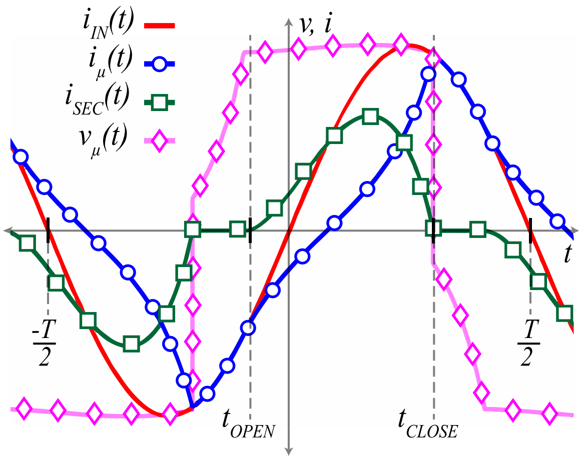

Fig. 5. Typical CTMEH circuit waveforms in **saturated** operation.

unconventional or transient load conditions. This analysis in this article is focused on “steady-state” dc voltage load behavior, as the buffered dc voltage load is relatively constant on a cycle-by-cycle basis of input current $i_{\text{IN}}(t)$ in many applications.

The main components of the CTMEH harvester are an ideal CT in parallel with a nonlinear magnetizing inductance. This nonlinear inductance is how we describe the saturating behavior of the harvester core so that load current, and thus power harvest can be calculated. The input current source $i_{\text{IN}}(t)$ is simply the current flowing through the primary wire divided according to the turns ratio of the CT. The magnetizing inductance swings between linear, unsaturated operation and nonlinear, saturated operation within each half cycle of input current, depending on the primary current conditions and the V_{LOAD} value connected to the core secondary winding. Our goal is to quantify the average power delivered to the dc voltage load as a function of harvesting setup conditions (e.g., I_P, ω), load conditions (e.g., V_{LOAD}), and harvester design parameters (e.g., μ_{eff}, B_{SAT}, secondary turns N, geometry). Therefore, an accurate description of the saturation timing of the magnetizing inductance and the current flowing through the magnetizing inductance $i_{\mu}(t)$ is needed such that $i_{\text{LOAD}}(t)$ can be expressed. Before diving into the mathematics of our nonlinear power harvest derivation, it is useful to first present and discuss the operating waveforms of the CTMEH circuit model depicted in Fig. 3. The circuit waveforms illustrate the key unknowns necessary to solve for CTMEH average power harvest calculations and highlight the distinction between an “unsaturated” and “saturated” core in this energy harvesting context.

Figs. 4 and 5 show simulated, typical circuit waveforms of a CTMEH terminated with a full bridge rectifier and constant dc voltage load. The power “transfer window,” coined in [11], is the portion of a half cycle of input current over which the secondary current $i_{\text{SEC}}(t)$ [and thus $i_{\text{LOAD}}(t)$] is nonzero. In unsaturated operation, the magnetizing inductance of the CTMEH is large and essentially constant. The transfer window length $t_{\text{CLOSE}} - t_{\text{OPEN}}$ is equal to a full $T/2$, with t_{OPEN} preceding the zero crossing of the input current by some small δ time period and t_{CLOSE} preceding $T/2$ by that same δ. Conversely, in saturated operation, the system is highly nonlinear. For the same input current, the transfer window length is notable shorter than a full $T/2$ half-cycle, as the magnetizing inductance becomes sufficiently saturated at t_{CLOSE} such that all of the input current begins to flow down the low impedance branch of the saturated magnetizing inductance, which acts as a short circuit. As a result, $i_{\mu}(t) = i_{\text{IN}}(t)$, and thus no current flows to the load until the core begins to exit saturation at the transfer window opening of the next half cycle. These waveforms illustrate several key features of the CTMEH circuit, which we refer to as “Observations.”

1) In **both unsaturated and saturated operation.**
   Observation 1: During the transfer window, one half of the full bridge rectifier is conducting, and thus the core voltage $v_{\mu}(t) = V_{\text{LOAD}} + 2V_d$.
   Observation 2: At the opening of the transfer window, the input current and magnetizing current are equal and begin to diverge: $i_{\text{IN}}(t_{\text{OPEN}}) = i_{\mu}(t_{\text{OPEN}})$.
   Observation 3: At the closing of the transfer window, the input current and magnetizing current are equal: $i_{\text{IN}}(t_{\text{CLOSE}}) = i_{\mu}(t_{\text{CLOSE}})$.
2) In **saturated operation only.**
   Observation 4: At the opening of the transfer window, the time derivatives of the input current and magnetizing current are equal: $\frac{\partial i_{\mu}(t)}{\partial t}\big|_{t=t_{\text{OPEN}}} = \frac{\partial i_{\text{IN}}(t)}{\partial t}\big|_{t=t_{\text{OPEN}}}$.
3) In **unsaturated operation only.**
   Observation 5: The transfer window length is a full $T/2$ long: $t_{\text{CLOSE}} - t_{\text{OPEN}} = \frac{T}{2}$.
   Observation 6: When t_{OPEN} precedes the $t = 0$ zero crossing of the input current by some δ, t_{CLOSE} precedes $t = T/2$ by the same δ.

These observations prove very powerful for providing additional equations and initial conditions necessary for solving the nonlinear power harvest model presented in the next section. These features of the CTMEH circuit, coupled with Faraday’s law, provide sufficient tools for solving for the bounds of the transfer window, the core magnetizing current, and the resulting average power harvest as a function of the voltage load level and of harvester design parameters.

III. Power Harvest Analysis

This section derives the average power harvest of a *hybrid* CTMEH. The overarching structure of our existing single-core CTMEH analysis method in [12] provides a logical basis for the derivation, but the hybrid harvester's cross-sectional inhomogeneity, multiple nonlinear flux density expressions, and resulting formula required for analyzing the hybrid, multicore harvester are novel. For succinctness and validation with practical experimental cores, the following derivation confines the general $n-$material hybrid core to a three-material hybrid core design of an inner magnetic material, a portion of air core, and an outer magnetic material. The general expression for the average power harvest of a CTMEH is

$$P_{\mathrm{LOAD}} = \frac{2}{T}\int_{t_{\mathrm{OPEN}}}^{t_{\mathrm{CLOSE}}} p_{\mathrm{LOAD}}(t)\,dt \tag{1}$$

where T is the period of primary current waveform, and $p_{\mathrm{LOAD}}(t)$ is the instantaneous power delivered to the load on the CTMEH secondary winding. As introduced in Section II, variables t_{OPEN} and t_{CLOSE} represent the opening and closing time respectively of the power transfer window during a half cycle of primary current over which the hybrid core magnetizing inductance is relatively unsaturated and delivering nonzero current to the secondary load.

Under constant voltage load conditions shown in Fig. 3, (1) can be rewritten as

$$P_{\mathrm{LOAD}} = \frac{2}{T}\int_{t_{\mathrm{OPEN}}}^{t_{\mathrm{CLOSE}}} i_{\mathrm{LOAD}}(t)\cdot V_{\mathrm{LOAD}}\,dt \tag{2}$$

where the constant load voltage can now be extracted from the integral, and $i_{\mathrm{LOAD}}(t)$ can be expressed in terms of input current and magnetizing current according to Kirchhoff's current law

$$P_{\mathrm{LOAD}} = \frac{2V_{\mathrm{LOAD}}}{T}\int_{t_{\mathrm{OPEN}}}^{t_{\mathrm{CLOSE}}} [i_{\mathrm{IN}}(t) - i_{\mu}(t)]\,dt \tag{3}$$

where we recognize that to predict P_{LOAD} for a given V_{LOAD}, we have three unknowns: t_{OPEN}, t_{CLOSE}, and $i_{\mu}(t)$ over the transfer window. The next three sections carry out detailed derivations to solve for each of these key variables as a function of the harvester design and circuit parameters. Our proposed general procedure first solves for the transfer window bounds under the assumption that the core is saturated. If the solutions yield a transfer window length that is not shorter than $T/2$, then the solutions are inconsistent with saturation behavior, and the bounds are recalculated under different, unsaturated assumptions in accordance with observations 5 and 6.

A. Solving for t_{OPEN}

From Faraday's law

$$v_{\mu}(t_{\mathrm{OPEN}}) = \left.\frac{\partial\lambda(t)}{\partial t}\right|_{t=t_{\mathrm{OPEN}}} \tag{4}$$

where λ is the total flux linkage of the CTMEH secondary winding. The total flux linkage of our N-turn, three-material hybrid CTMEH is

$$\lambda(t) = N\,h\left[\int_{r_0}^{r_1}\vec{B}_{\mathrm{IN}}(t)\cdot d\vec{r} + \int_{r_1}^{r_2}\vec{B}_{\mathrm{AIR}}(t)\cdot d\vec{r} + \int_{r_2}^{r_3}\vec{B}_{\mathrm{OUT}}(t)\cdot d\vec{r}\right] \tag{5}$$

where we assume the flux density does not vary with significantly with r inside the regions of the hybrid core that are the same material [27]. Thus, (5) can be simplified as

$$\lambda(t) = N\,h\,[(r_1 - r_0)\,B_{\mathrm{IN}}(t) + (r_2 - r_1)\,B_{\mathrm{AIR}}(t) + (r_3 - r_2)\,B_{\mathrm{OUT}}(t)]\,. \tag{6}$$

This simplifying assumption of uniform flux density within the same core material is a potential source of error for more complex harvester geometries. In such cases, a designer should more finely discretize the radial flux density integral, perhaps even within the same core material, to smaller regions over which the homogeneous flux density assumption accurately holds. In the limit, one essentially creates a fine 1-D finite element mesh of the radial geometry, but simplifying assumptions of $B(t)$ uniformity within the same material yield a reduced order model that is convenient for efficient analysis. According to observation 1, at $t = t_{\mathrm{OPEN}}$ the load current is just beginning to become nonzero, and therefore two of the diodes in the full bridge rectifier are conducting. The magnetizing inductance voltage is thus

$$v_{\mu}(t_{\mathrm{OPEN}}) = V_{\mathrm{LOAD}} + 2V_d. \tag{7}$$

Combining (4), (6), and (7) gives

$$V_{\mathrm{LOAD}} + 2V_d = N\,h\,\frac{\partial}{\partial t}\,[(r_1 - r_0)\,B_{\mathrm{IN}}(t) + (r_2 - r_1)\,B_{\mathrm{AIR}}(t) + (r_3 - r_2)\,B_{\mathrm{OUT}}(t)]\Big|_{t=t_{\mathrm{OPEN}}} \tag{8}$$

where we can now distribute the partial derivative to each $B(t)$ term since the derivative is a linear operator

$$V_{\mathrm{LOAD}} + 2V_d = N\,h\left[(r_1 - r_0)\,\frac{\partial B_{\mathrm{IN}}(t)}{\partial t} + (r_2 - r_1)\,\frac{\partial B_{\mathrm{AIR}}(t)}{\partial t} + (r_3 - r_2)\,\frac{\partial B_{\mathrm{OUT}}(t)}{\partial t}\right]\Bigg|_{t=t_{\mathrm{OPEN}}} \tag{9}$$

where a flux density formula should be plugged into each $B(t)$ term in (9). Our previous work has discussed the details of mapping sigmoid functions, the family of "S-shaped" curves to $B-H$ magnetization curves for the purpose of describing highly nonlinear saturating core behavior [27]. Since this article focuses on deriving analytical formula from which key CTMEH power harvest variables ($t_{\mathrm{OPEN}}, t_{\mathrm{CLOSE}}, i_{\mu}(t)$) can be solved, we also emphasize that this function be differentiable such that each $B(t)$ term can be analytically differentiated when plugged into (9). Specifically, we use

$$B_{\text{IN}}(t) = B_{\text{SAT1}} \frac{2}{\pi} \text{arctan} \left(\frac{\pi N \mu_{\text{eff1}} \mu_0}{2\, l_{\text{IN}}\, B_{\text{SAT1}}} i_\mu(t) \right) \tag{10}$$

$$B_{\text{AIR}}(t) = \mu_0 \frac{N}{l_{\text{AIR}}} i_\mu(t) \tag{11}$$

$$B_{\text{OUT}}(t) = B_{\text{SAT2}} \frac{2}{\pi} \text{arctan} \left(\frac{\pi N \mu_{\text{eff2}} \mu_0}{2\, l_{\text{OUT}}\, B_{\text{SAT2}}} i_\mu(t) \right) \tag{12}$$

as our flux density functions, where l_{IN}, l_{AIR}, and l_{OUT} are the mean magnetic path lengths of the inner core, air region, and outer core, respectively. We consider effective initial relative permeability μ_{eff} and saturation flux density B_{SAT} to be constant; however, it is important to note that such properties may vary as a function of practical environmental conditions, such as temperature. "High performing" CTMEH materials (e.g., si-steel [29] and nanocrystalline alloys [29], [30]) have Curie temperatures well above 500°C, and thus the thermal limitations of downstream circuitry, such as supercapacitors and integrated circuits, are the system elements limiting the appropriate operating range for practical CTMEH systems. Within this limited temperature range, a designer should reference appropriate core material specification sheets (e.g., VAC VITROPERM 500/800 [30]) to update material property parameters accordingly for refined modeling. Our chosen, nonlinear $B(t)$ arctangent function has been validated in many previous works [11], [12], [23], [27] and is conveniently differentiable for our following analysis. Plugging (10), (11), and (12) into (9) and carrying out the differentiation gives

$$\begin{aligned} &V_{\text{LOAD}} + 2V_d = \\ &N\,h \left[(r_1 - r_0) \left(\frac{\frac{\mu_{\text{eff1}} \mu_0 N}{l_{\text{IN}}}}{1 + (i_\mu(t))^2 (\frac{\pi \mu_{\text{eff1}} \mu_0 N}{2\, l_{\text{IN}} B_{\text{SAT1}}})^2} \frac{\partial i_\mu(t)}{\partial t} \right) \Big|_{t=t_{\text{OPEN}}} \right. \\ &+ \ (r_2 - r_1) \frac{\mu_0 N}{l_{\text{AIR}}} \left(\frac{\partial i_\mu(t)}{\partial t} \right) \Big|_{t=t_{\text{OPEN}}} \\ &\left. + \ (r_3 - r_2) \left(\frac{\frac{\mu_{\text{eff2}} \mu_0 N}{l_{\text{OUT}}}}{1 + (i_\mu(t))^2 (\frac{\pi \mu_{\text{eff2}} \mu_0 N}{2\, l_{\text{OUT}} B_{\text{SAT2}}})^2} \frac{\partial i_\mu(t)}{\partial t} \right) \Big|_{t=t_{\text{OPEN}}} \right]. \end{aligned} \tag{13}$$

Here, we can leverage observations 2 and 4 to reduce number of unknowns in (13). Specifically at $t = t_{\text{OPEN}}$ in the saturated case, both the magnetizing current and its time derivative are equal to the input current and the input current's time derivative respectively. Mathematically, we have

$$i_\mu(t_{\text{OPEN}}) = i_{\text{IN}}(t_{\text{OPEN}}) = \frac{I_P}{N} \sin(\omega t_{\text{OPEN}}) \tag{14}$$

$$\frac{\partial i_\mu(t)}{\partial t}\Big|_{t=t_{\text{OPEN}}} = \frac{\partial i_{\text{IN}}(t)}{\partial t}\Big|_{t=t_{\text{OPEN}}} = \omega \frac{I_P}{N} \cos(\omega t_{\text{OPEN}}) \tag{15}$$

which allows the $i_\mu(t)$ and $\partial i_\mu(t)/\partial t$ terms to be expressed purely in terms of primary side current information (I_P, ω) and a design variable (N), the number of secondary turns. Substituting (14) and (15) into (13) gives

$$\begin{aligned} &V_{\text{LOAD}} + 2V_d = \\ &N\,h \left[(r_1 - r_0) \frac{\frac{\mu_{\text{eff1}} \mu_0}{l_{\text{IN}}} \omega I_P \cos(\omega t_{\text{OPEN}})}{1 + (\frac{I_P}{N} \sin(\omega t_{\text{OPEN}}))^2 (\frac{\pi \mu_{\text{eff1}} \mu_0 N}{2\, l_{\text{IN}} B_{\text{SAT1}}})^2} \right. \\ &+ \ (r_2 - r_1) \frac{\mu_0}{l_{\text{AIR}}} \omega I_P \cos(\omega t_{\text{OPEN}}) \\ &\left. + \, (r_3 - r_2) \frac{\frac{\mu_{\text{eff2}} \mu_0}{l_{\text{OUT}}} \omega I_P \cos(\omega t_{\text{OPEN}})}{1 + (\frac{I_P}{N} \sin(\omega t_{\text{OPEN}}))^2 (\frac{\pi \mu_{\text{eff2}} \mu_0 N}{2\, l_{\text{OUT}} B_{\text{SAT2}}})^2} \right] \end{aligned} \tag{16}$$

a single equation with one unknown, t_{OPEN}. (16) is a transcendental equation with no closed form solution for t_{OPEN}, but this equation can be solved numerically to get an accurate estimate of the transfer window opening time.

After obtaining a solution for t_{OPEN}, we can recognize that $i_\mu(t_{\text{OPEN}})$ is now also a known numerical quantity, since, according to observation 2, the magnetizing current and input current are equal at $t = t_{\text{OPEN}}$. Furthermore, our three flux density expressions $[B_{\text{IN}}(t)$, $B_{\text{AIR}}(t)$, and $B_{\text{OUT}}(t)]$ given in (10)–(12) respectively are functions of $i_\mu(t)$, core design and material parameters, and primary side current information. Thus, at this stage of the derivation, since $i_\mu(t_{\text{OPEN}})$ is known, then $B_{\text{IN}}(t_{\text{OPEN}})$, $B_{\text{AIR}}(t_{\text{OPEN}})$, and $B_{\text{OUT}}(t_{\text{OPEN}})$ are all known quantities. This observation proves very useful, as it will allow for the reduction of unknown terms in the equation for solving for the closing time of the power transfer window.

B. *Solving for t_{CLOSE}*

Expressing Faraday's law in terms of core voltage integration gives

$$\Delta\lambda = \lambda(t_{\text{CLOSE}}) - \lambda(t_{\text{OPEN}}) = \int_{t_{\text{OPEN}}}^{t_{\text{CLOSE}}} v_\mu(t)\, dt. \tag{17}$$

According to observation 1, the core voltage over the transfer window $v_\mu(t)$ is approximately constant and equal to the dc voltage load plus 2 rectifier diode forward voltage drops. The $\lambda(t_{\text{CLOSE}})$ and $\lambda(t_{\text{OPEN}})$ of (17) can also be alternatively expressed in terms of harvester geometry (r_i, h), secondary turns, and flux density expressions. Therefore, (17) can be rewritten as

$$\begin{aligned} N\,h \Big\{ &\Big[(r_1 - r_0)\, B_{\text{IN}}(t_{\text{CLOSE}}) \\ &+ \ (r_2 - r_1)\, B_{\text{AIR}}(t_{\text{CLOSE}}) \\ &+ \ (r_3 - r_2)\, B_{\text{OUT}}(t_{\text{CLOSE}}) \Big] \\ &- \\ &\Big[(r_1 - r_0)\, B_{\text{IN}}(t_{\text{OPEN}}) \\ &+ \ (r_2 - r_1)\, B_{\text{AIR}}(t_{\text{OPEN}}) \end{aligned}$$

$$\begin{aligned} &+\ (r_3 - r_2)\, B_{\text{OUT}}(t_{\text{OPEN}})\Big]\Bigg\} \\ &= (V_{\text{LOAD}} + 2V_d)(t_{\text{CLOSE}} - t_{\text{OPEN}}). \end{aligned} \tag{18}$$

Here, it should be emphasized that each of the flux density terms at t_{OPEN} are known at this stage of the derivation, as discussed at the end of Section III-A. To condense terms we will call

$$\begin{aligned} &\Big[(r_1 - r_0)\, B_{\text{IN}}(t_{\text{OPEN}}) \\ &+\ (r_2 - r_1)\, B_{\text{AIR}}(t_{\text{OPEN}}) \\ &+\ (r_3 - r_2)\, B_{\text{OUT}}(t_{\text{OPEN}})\Big] \\ &= C_{\text{OPEN}}. \end{aligned} \tag{19}$$

Expressing each $B(t_{\text{CLOSE}})$ term as its arctangent flux density description and employing observation 3 to represent $i_\mu(t_{\text{CLOSE}}) = i_{\text{IN}}(t_{\text{CLOSE}}) = \frac{I_P}{N}\sin(\omega t_{\text{CLOSE}})$ purely in terms of primary side information gives

$$\begin{aligned} N\,h\,\Bigg\{&\Bigg[(r_1 - r_0)\, B_{\text{SAT1}}\frac{2}{\pi}\arctan\left(\frac{\pi \mu_{\text{eff1}}\mu_0 I_P}{2 l_{\text{IN}} B_{\text{SAT1}}}\sin(\omega t_{\text{CLOSE}})\right) \\ &+\ (r_2 - r_1)\,\frac{\mu_0 I_P}{l_{\text{AIR}}}\sin(\omega t_{\text{CLOSE}}) \\ &+ (r_3 - r_2)\, B_{\text{SAT2}}\frac{2}{\pi}\arctan\left(\frac{\pi \mu_{\text{eff2}}\mu_0 I_P}{2 l_{\text{OUT}} B_{\text{SAT2}}}\sin(\omega t_{\text{CLOSE}})\right)\Bigg] \\ &- C_{\text{OPEN}}\Bigg\} \\ &= (V_{\text{LOAD}} + 2V_d)(t_{\text{CLOSE}} - t_{\text{OPEN}}). \end{aligned} \tag{20}$$

Here, (20) has one unknown, t_{CLOSE}, as desired, but (20) is also a transcendental equation with no closed form solution. Again, a numerical solver can approximate a valid solution for t_{CLOSE} according to (20). At this point, the bounds of the transfer window have been solved assuming the core underwent saturation in the half cycle of primary current. Before proceeding to a calculation of magnetizing current and resulting average power harvest, one must first check that the core was in fact saturated.

C. *Unsaturated Solutions*

In the event that the above-mentioned solutions yield a transfer window length $t_{\text{CLOSE}} - t_{\text{OPEN}} \geq \frac{T}{2}$, then our transfer window solution bounds violate the assumption that the core was saturated. Therefore, the transfer window bounds must be resolved for under different assumptions, exploiting the unsaturated Observations presented previously in Section II. According to observation 5, an unsaturated transfer window length is a full half cycle long

$$t_{\text{CLOSE}} - t_{\text{OPEN}} = \frac{T}{2}. \tag{21}$$

Furthermore, as stated in observation 6, if t_{OPEN} precedes $t = 0$ by some δ, then t_{CLOSE} precedes $t = T/2$ by that same δ as the unsaturated core operates in a half wave symmetric fashion. Thus, in the unsaturated regime

$$i_\mu(t_{\text{OPEN}}) = -i_\mu(t_{\text{CLOSE}}) \tag{22}$$

$$\Rightarrow B(t_{\text{OPEN}}) = -B(t_{\text{CLOSE}}) \tag{23}$$

$$\Rightarrow \lambda(t_{\text{OPEN}}) = -\lambda(t_{\text{CLOSE}}). \tag{24}$$

Under these new assumptions, Faraday's law can be rewritten as follows:

$$\begin{aligned} \Delta\lambda = \lambda(t_{\text{CLOSE}}) - \lambda(t_{\text{OPEN}}) &= \int_{t_{\text{OPEN}}}^{t_{\text{CLOSE}}} v_\mu(t)\, dt \\ \Rightarrow -2\lambda(t_{\text{OPEN}}) &= (V_{\text{LOAD}} + 2V_d)\left(\frac{T}{2}\right). \end{aligned} \tag{25}$$

Re-expressing (25) in terms of flux densities gives

$$\begin{aligned} &-N\,h\,\Big[(r_1 - r_0)\, B_{\text{IN}}(t_{\text{OPEN}}) \\ &+\ (r_2 - r_1)\, B_{\text{AIR}}(t_{\text{OPEN}}) \\ &+\ (r_3 - r_2)\, B_{\text{OUT}}(t_{\text{OPEN}})\Big] \\ &= (V_{\text{LOAD}} + 2V_d)\left(\frac{T}{4}\right) \end{aligned} \tag{26}$$

and substituting our arctangent descriptions for the flux density terms yields

$$\begin{aligned} -N\,h\,\Bigg[&(r_1 - r_0)\, B_{\text{SAT1}}\frac{2}{\pi}\arctan\left(\frac{\pi N \mu_{\text{eff1}}\mu_0}{2\, l_{\text{IN}}\, B_{\text{SAT1}}} i_\mu(t_{\text{OPEN}})\right) \\ &+\ (r_2 - r_1)\,\mu_0\frac{N}{l_{\text{AIR}}} i_\mu(t_{\text{OPEN}}) \\ &+\ (r_3 - r_2)\, B_{\text{SAT2}}\frac{2}{\pi}\arctan\left(\frac{\pi N \mu_{\text{eff2}}\mu_0}{2\, l_{\text{OUT}}\, B_{\text{SAT2}}} i_\mu(t_{\text{OPEN}})\right)\Bigg] \\ &= (V_{\text{LOAD}} + 2V_d)\left(\frac{T}{4}\right). \end{aligned} \tag{27}$$

According to observation 2, in either unsaturated or saturated operation the magnetizing current and input current are equal at $t = t_{\text{OPEN}}$

$$i_\mu(t_{\text{OPEN}}) = i_{\text{IN}}(t_{\text{OPEN}}) = \frac{I_P}{N}\sin(\omega t_{\text{OPEN}}). \tag{28}$$

Substituting (28) into (27) gives the following one equation with a single unknown, t_{OPEN}:

$$\begin{aligned} -N\,h\,\Bigg[&(r_1 - r_0)\, B_{\text{SAT1}}\frac{2}{\pi}\arctan\left(\frac{\pi \mu_{\text{eff1}}\mu_0 I_P}{2\, l_{\text{IN}}\, B_{\text{SAT1}}}\sin(\omega t_{\text{OPEN}})\right) \\ &+\ (r_2 - r_1)\,\mu_0\frac{N}{l_{\text{AIR}}} i_\mu(t_{\text{OPEN}}) \\ &+\ (r_3 - r_2)\, B_{\text{SAT2}}\frac{2}{\pi}\arctan\left(\frac{\pi \mu_{\text{eff2}}\mu_0 I_P}{2\, l_{\text{OUT}}\, B_{\text{SAT2}}}\sin(\omega t_{\text{OPEN}})\right)\Bigg] \\ &= (V_{\text{LOAD}} + 2V_d)\left(\frac{T}{4}\right). \end{aligned} \tag{29}$$

Once again, a numerical solver can solve the above-mentioned equation for t_{OPEN} in the unsaturated case. Since we are in unsaturated operation, t_{CLOSE} is simply $t_{\text{OPEN}} + T/2$ according to observation 5.

D. Solving for $i_\mu(t)$

With the bounds of the transfer window now known, the remaining task is to solve for the magnetizing current over the transfer window. Observation 1 states that $v_\mu = V_{\text{LOAD}} + 2V_d$ over the transfer window. Generally, according to Faraday's law

$$v_\mu(t) = \frac{\partial \lambda(t)}{\partial t}. \tag{30}$$

The partial derivative of the flux linkage, specifically at t_{OPEN}, was already evaluated in (13) previously, but can now be expressed more generally in time

$$\begin{aligned} &V_{\text{LOAD}} + 2V_d = \\ &N\,h\left[(r_1 - r_0)\,\frac{\frac{\mu_{\text{eff1}}\mu_0 N}{l_{\text{IN}}}}{1 + (i_\mu(t))^2\left(\frac{\pi\mu_{\text{eff1}}\mu_0 N}{2\,l_{\text{IN}}B_{\text{SAT1}}}\right)^2}\,\frac{\partial i_\mu(t)}{\partial t}\right. \\ &\quad +\ (r_2 - r_1)\,\frac{\mu_0 N}{l_{\text{AIR}}}\left(\frac{\partial i_\mu(t)}{\partial t}\right) \\ &\quad \left. +\ (r_3 - r_2)\,\frac{\frac{\mu_{\text{eff2}}\mu_0 N}{l_{\text{OUT}}}}{1 + (i_\mu(t))^2\left(\frac{\pi\mu_{\text{eff2}}\mu_0 N}{2\,l_{\text{OUT}}B_{\text{SAT2}}}\right)^2}\,\frac{\partial i_\mu(t)}{\partial t}\right]. \end{aligned} \tag{31}$$

Equation (31) is a first order nonlinear ordinary differential equation (ODE) for $i_\mu(t)$ over the transfer window. Observation 2 provides the following initial condition:

$$i_\mu(t_{\text{OPEN}}) = i_{\text{IN}}(t_{\text{OPEN}}) = \frac{I_P}{N}\sin(\omega t_{\text{OPEN}}) \tag{32}$$

to solve for $i_\mu(t)$ over the transfer window. This nonlinear ODE can be solved using numerical tools, such that the solution can be integrated numerically in our final power harvest calculation described in Section III-E.

E. Average Power Harvest

With solutions for $t_{\text{OPEN}}, t_{\text{CLOSE}}$, and an expression with an initial condition for $i_\mu(t)$ over the transfer window, a designer now has all the information necessary to numerically calculate the CTMEH average power harvest according to (3). Splitting the integration of the current difference as written in (3) into a difference of integrated currents gives

$$P_{\text{LOAD}} = \frac{2V_{\text{LOAD}}}{T}\left[\int_{t_{\text{OPEN}}}^{t_{\text{CLOSE}}} i_{\text{IN}}(t)\,dt - \int_{t_{\text{OPEN}}}^{t_{\text{CLOSE}}} i_\mu(t)\,dt\right]. \tag{33}$$

The input current is simply the primary current divided by the turns ratio of the CTMEH. Substituting in yields

$$P_{\text{LOAD}} = \frac{2V_{\text{LOAD}}}{T}\left[\int_{t_{\text{OPEN}}}^{t_{\text{CLOSE}}} \frac{I_P}{N}\sin(\omega t)\,dt\right. \tag{34}$$

$$\left. - \int_{t_{\text{OPEN}}}^{t_{\text{CLOSE}}} i_\mu(t)\,dt\right] \tag{35}$$

where the first integral can be explicitly calculated analytically. Carrying out that integration we have a key result

$$\begin{aligned} P_{\text{LOAD}} = \frac{2V_{\text{LOAD}}}{T}&\left[\frac{1}{\omega}\frac{I_P}{N}\left(\cos(\omega t_{\text{OPEN}}) - \cos(\omega t_{\text{CLOSE}})\right)\right. \\ &\left. - \int_{t_{\text{OPEN}}}^{t_{\text{CLOSE}}} i_\mu(t)\,dt\right]. \end{aligned} \tag{36}$$

At this final stage, $i_\mu(t)$ can be integrated numerically from t_{OPEN} to t_{CLOSE} using the ODE of (31) and its initial condition (32) to obtain a final, average power harvest calculation.

Our proposed analytical model presented in this section is a useful tool for quickly predicting the average power harvest of a saturating, hybrid CTMEH over a wide voltage load sweep. Contrary to running a full, nonlinear time-domain numerical circuit simulation or 3-D finite element method solver to model power harvest, our framework reduces the saturating CTMEH problem to a few nonlinear numerical solves and one final numerical integration to solve for average power harvest using (36). This model reduction is especially useful for optimization-based hybrid CTMEH design as it can significantly shorten the total design cycle time when evaluating very many proposed CTMEH design variants.

IV. MODEL REFINEMENTS

The modeling of Section III provides great utility to a CTMEH designer. Building from the multiterm flux description of (6), we derived and solved for the resulting P_{LOAD} of a hybrid harvester design with a limited system of equations and few numerical solves. In addition, one can employ a nonlinear flux description of the form of (6) in SPICE to augment the modeling process for a more refined design. Parasitic elements, for example, such core losses, fringing fields, and leakage inductance, are not captured in our modeling of Section III previously and are therefore potential sources of error. Numerical SPICE tools are an excellent means of supplementing the reduced order analysis of Section III to further sharpen designs including parasitic elements and also to easily test different $B - H$ magnetization curve sigmoid functions using nonlinear inductor models.

A circuit model, including loss elements, of a CTMEH is shown in Fig. 6, where a generic "load" is shown across the harvester secondary winding. R_{CORE}, L_{LEAK}, and R_{WIRE} represent the equivalent core loss resistance, leakage inductance, and secondary winding dc wire resistance, respectively. Our recent publication implemented this circuit model in SPICE using multiterm flux descriptions in the form of (6) and validated the circuit model against experimental hybrid core designs under a variety of resistive load conditions [27]. SPICE modeling of a hybrid CTMEH circuit enables the inclusion and sweeping of parasitic parameters as well as the ability to test the CTMEH circuit with more complex, power electronic secondary loads or under unconventional, varying, or multifrequency primary current excitations. Such modeling is also a reliable means of

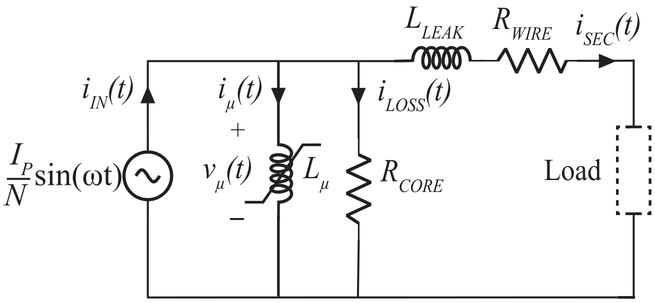

Fig. 6. Electric circuit model of CTMEH including parasitics.

TABLE II
EXPERIMENTAL HARVESTER PARAMETERS

Parameter	Hybrid H1	Hybrid H2
Inner core material	Si-Steel	Nanocrystalline
Outer core material	Nanocrystalline	Si-Steel
Secondary turns	100	
r_0 [mm]	9	
r_1 [mm]	14	
r_2 [mm]	16	
r_3 [mm]	21	
h [mm]	20	

exploring the sensitivity of power harvest to design parameters, such as μ_{eff}. For example, our existing work employed the hybrid core SPICE model to reveal the importance of modeling core loss at "low" primary currents, the high sensitivity of power harvest to μ_{eff} at low primary currents, and the competing accuracies of the $\tanh(x)$ versus $\arctan(x)$ nonlinear flux descriptions for hybrid core modeling [27]. Similarly, a designer could use the SPICE model to sweep leakage inductance and saturation flux density to explore their relative effects on resulting power harvest. In summary, our analytical model that is the primary focus of this article provides a fast and accurate means of approximating the power harvest of a given design, and SPICE modeling can augment the design process to tune a coarser design for capturing the effects of parasitic elements.

V. EXPERIMENTAL VALIDATION

Two hybrid cores, denoted "H1" and "H2" were constructed to validate our power harvest model and demonstrate harvester performance of each hybrid core design. The hybrid harvesters were assembled from concentric, split toroids: one si-steel and one nanocrystalline alloy, with a small air core region between these inner and outer cores, yielding "three-material" experimental harvesters. The hybrid harvester designs are identical to each other aside from the ordering of the inner and outer magnetic materials in the hybrid assembly. The experimental harvester details are included in Table II.

Each hybrid harvester was tightly clamped around 1 turn of a primary wire for power harvest experimentation. A KEPCO BOP-MG power supply, configured as a current source, provided a 60 Hz ac sinusoidal current through the primary wire. Each harvester was tested at primary current levels of 5.0, 10.0, 20.0, 30.0, and 50.0 A_{rms}. The harvester secondary winding was terminated with a full bridge rectifier of four discrete MBR0520 Schottky diodes followed by a dc voltage load. A loaded Agilent U8032A dc power supply acted as the dc voltage load, and the dc voltage was swept over a wide range at each primary current level to subject the core to varying degrees of saturation. A Keysight InfiniiVision DSOX4154A oscilloscope was used for the primary current and output load power measurements. Output power measurements (load voltage and load current) were made on the dc side of the rectifier stage, with one oscilloscope channel measuring the dc load voltage level and another oscilloscope channel measuring load current through a low-side current sense resistor. An annotated photograph of the experimental setup is shown in Fig. 7.

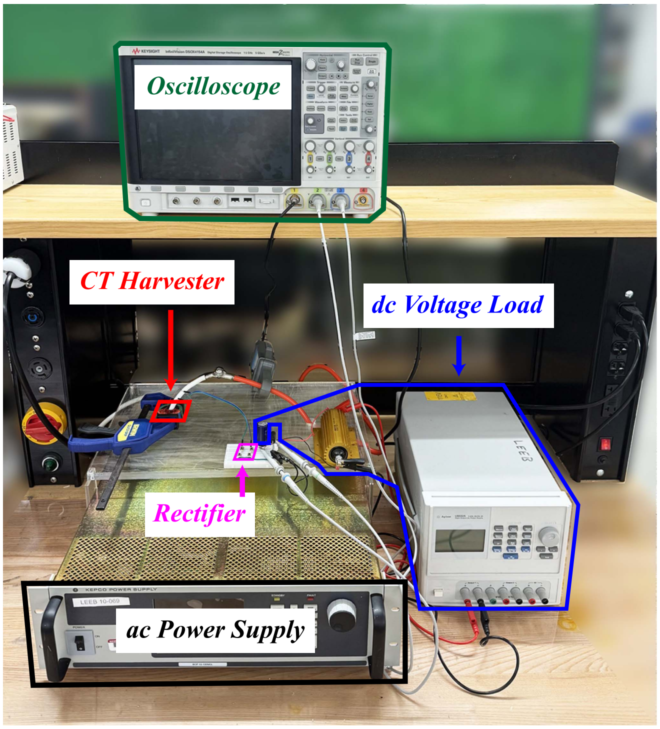

Fig. 7. Annotated photograph of CTMEH experimental setup.

Our proposed analytical model was implemented in Python, using standard SciPy library functions to perform the necessary nonlinear numerical solves and integration for calculating average power harvest P_{LOAD}. Since our analytical model requires a few numerical solves, we refer to it as the "semianalytical model" in our results of this section. This semianalytical power harvest model was run for a wide sweep of V_{LOAD} levels, predicting a P_{LOAD} for each V_{LOAD} along the sweep for validation against experimental data. In the modeling, the rectifier diode forward voltage drop parameter V_d was varied based on the V_{LOAD} level to account for the significant reduction in average forward current carried through the rectifier at higher V_{LOAD} values that drive the core into more aggressive saturation. The harvester magnetic material parameters used in our modeling are recorded in Table III, where μ_{eff} parameters were varied within nominal ranges depending on the primary current test level to yield good agreement with experimental data.

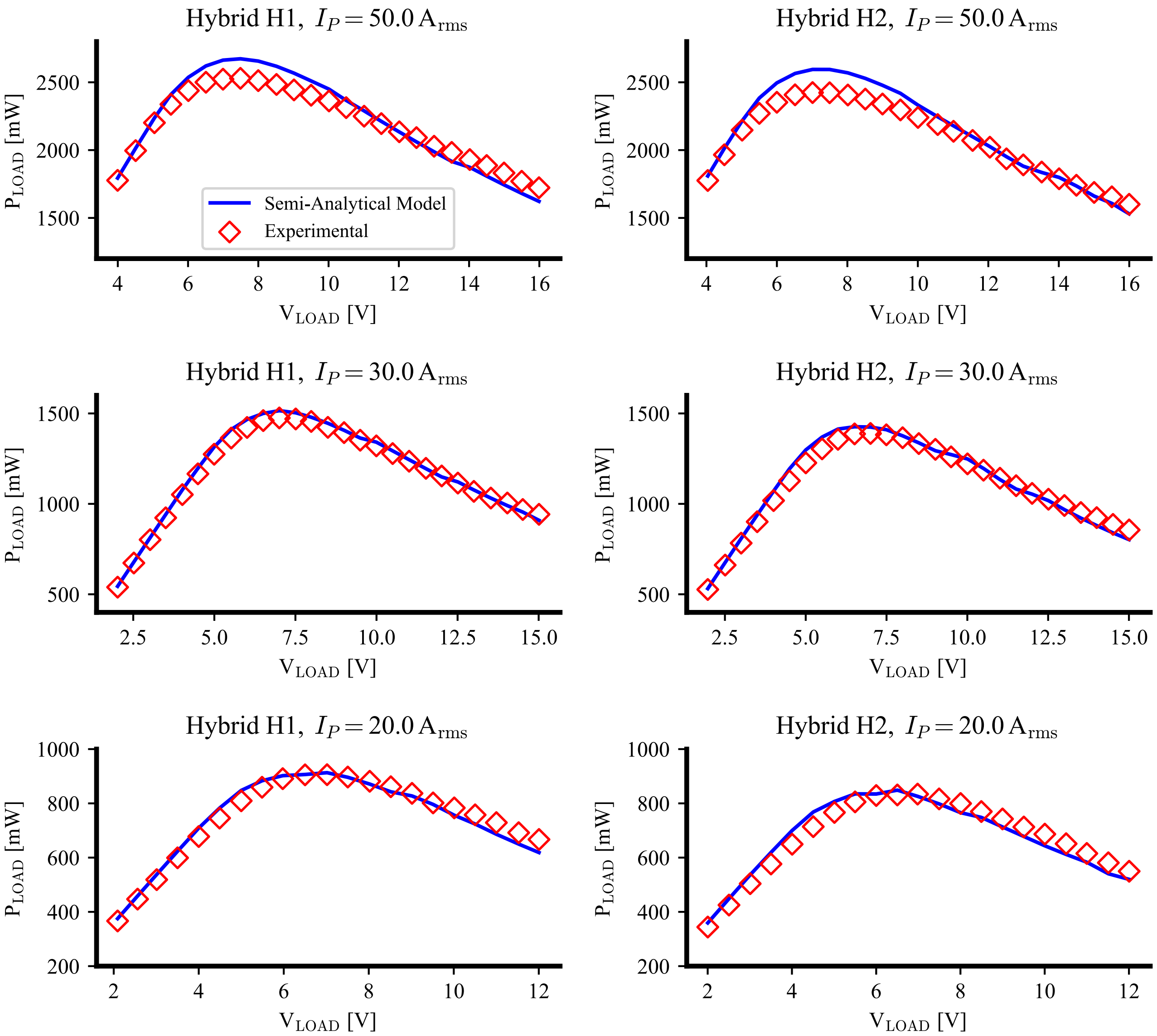

Fig. 8. Experimental power harvest data for both the H1 and H2 harvesters agrees well with the predictions of the mathematical model over a wide primary current range.

TABLE III
SEMIANALYTICAL MODEL MAGNETIC PARAMETERS

Parameter	Hybrid H1	Hybrid H2
μ_{eff1} [unitless]	12 000−15 000	27 000−30 000
B_{SAT1} [T]	2.0	1.2
μ_{eff2} [unitless]	22 000−28 000	13 000−16 000
B_{SAT2} [T]	1.2	2.0

TABLE IV
MAXIMUM PERCENT ERROR BETWEEN SEMIANALYTICAL MODEL AVERAGE POWER HARVEST AND EXPERIMENTAL AVERAGE POWER HARVEST

I_P [$\mathrm{A_{rms}}$]	Maximum percent error [%]	
	Hybrid H1	Hybrid H2
50.0 $\mathrm{A_{rms}}$	5.85%	7.08%
30.0 $\mathrm{A_{rms}}$	3.52%	6.28%
20.0 $\mathrm{A_{rms}}$	7.23%	7.81%

Fig. 8 shows the strong modeling agreement between the semianalytical model and experimental power harvest data for hybrid H1 and hybrid H2 at the 20.0, 30.0, and 50.0 $\mathrm{A_{rms}}$ primary current conditions. The maximum percent errors of each dataset, defined with respect to the experimental P_{LOAD} values are recorded in Table IV. These results demonstrate the accuracy and reliability of the proposed semianalytical model for describing nonlinear, saturating, hybrid CTMEH behavior across a wide primary current range.

As discussed in Section IV and in our recent hybrid core publication [27], parasitic properties, such as core loss, and alternative nonlinear sigmoid functions for describing saturation behavior, such as hyperbolic tangent instead of arctangent, can become critical for accurate power harvest modeling, especially at low primary currents. This is because core loss contributes to a larger fraction of the total average power harvest under low current conditions and because the minor, nonlinear magnetization loop

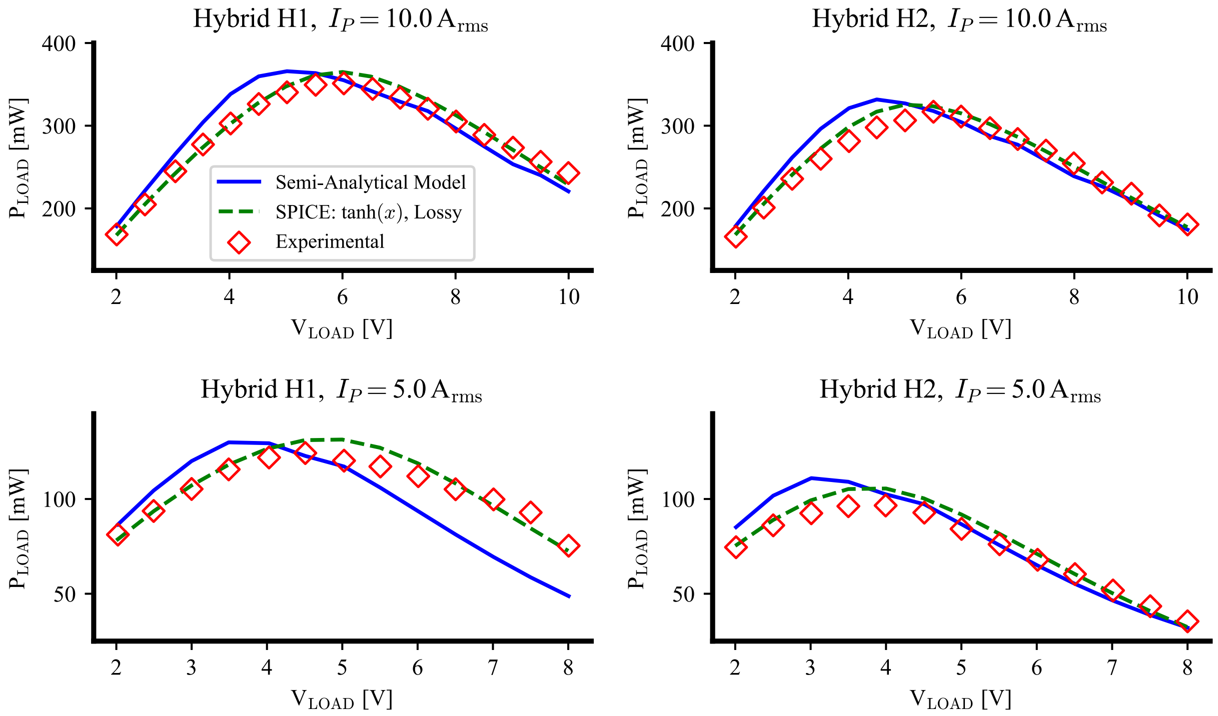

Fig. 9. Under lower current excitations, SPICE modeling incorporating core loss and a tanh(x) nonlinear inductance description more accurately describes the saturating hybrid harvesters.

over which a CTMEH operates may be more accurately tracked by an alternative sigmoid function depending on the primary current conditions and chosen core materials.

Fig. 9 shows the results of the semianalytical model and experimental power harvest for the "low" 5.0 and 10.0 $\mathrm{A_{rms}}$ primary current tests. In addition, Fig. 9 overlays a P_{LOAD} curve for the modeled average power harvest output of a CTMEH SPICE simulation using the lossy circuit model described in Section IV. Specifically, the SPICE simulations implemented the nonlinear, saturating hybrid core inductance with hyperbolic tangent $B(t)$ functions, further μ_{eff} parameter value adjustments, and a nonnegligible R_{CORE} equivalent core loss resistance. Due to the simplifying assumptions of our semianalytical model, the maximum percent errors between the semianalytical model and experimental power harvest, again defined with respect to the experimental power harvest, grow significantly under low current excitations. The maximum errors are 11.78% and 36.83% for H1 at the 10.0 and 5.0 $\mathrm{A_{rms}}$ I_P tests, respectively. For H2, the maximum percent errors at 10.0 and 5.0 $\mathrm{A_{rms}}$ are 14.18% and 20.04%, respectively. Alternatively, as proposed in Section IV and consistent with our recent work [27], adjusting the magnetization curve descriptions to hyperbolic tangent in SPICE and incorporating an equivalent core loss resistance into the model can correct for the simplified model's disagreement. As shown in Fig. 9, the power harvest of the lossy, refined SPICE model better track the experimental data under these low current conditions. The SPICE curves exhibit maximum percent errors with respect to the experimental data of 5.80% and 9.27% for H1 and 6.37% and 9.41% for H2 at 10.0 and 5.0 $\mathrm{A_{rms}}$, respectively.

At each experimental I_P, H1 outperforms H2 in terms of maximum P_{LOAD}. Consistent with existing literature [11], [12], [23], each harvester exhibits a P_{LOAD} that linearly increases with V_{LOAD} in the unsaturated regime at "low" voltage loads, a P_{LOAD} that decreases at larger voltage loads which deeply saturate the core, and a maximum P_{LOAD} in soft saturation, at a "Goldilocks" V_{LOAD} between the unsaturated and hard saturated voltage load levels.

VI. DISCUSSION

This section further discusses the experimental results previously and addresses implications of hybrid core performance and design. Although H1 outperforms H2 at all currents tested in the experimental dataset, an interesting feature of these hybrid harvesters is the change in their comparative performance depending on the primary current operating condition. Our recent publication [27], presented a direct comparison of single-material nanocrystalline and si-steel cores against hybrid core designs, highlighting the ability of hybrid cores to harvest well over a wide range of primary currents in contrast to the single-material harvesters that only perform well within a limited range of primary currents. A key, natural design question for a hybrid CTMEH is the choice of ordering for the inner and outer core materials. Should the "high μ_{eff}, low B_{SAT}" material be the inner core and the "low μ_{eff}, high B_{SAT}" material be the outer core, or vice versa? Our analysis and results indicate that the order of materials is paramount at lower primary currents, but does not have a significant effect on comparative performance at high primary currents.

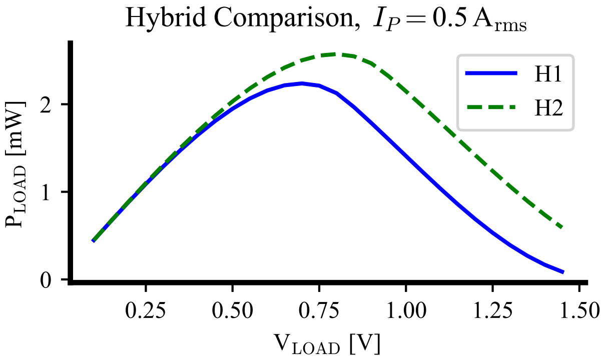

Fig. 10. At very low primary currents, the H2 hybrid design out-harvests the H1 design.

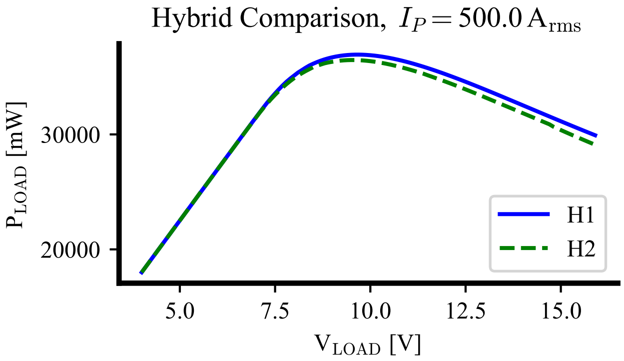

Fig. 11. At very high primary currents, the ordering of inner and outer core materials in a hybrid design has little effect on average power harvest.

Recalling the simulation results of Table I, we observed that the 9.5767 mW P_{MAX} of H2 *exceeded* the 8.6917 mW P_{MAX} of H1 in an $I_P = 1.0$ A$_{\text{rms}}$ simulation. At our 5.0, 10.0, 20.0, 30.0, and 50.0 A$_{\text{rms}}$ primary current experimental test conditions, we saw H1 maximum power harvests that exceeded those of H2, but with diminishing returns as I_P increased. H1's P_{MAX} at $I_P = 5.0$ A$_{\text{rms}}$ was 128.65% that of H2, but became 110.82% the maximum power harvest of H2 at 10.0 A$_{\text{rms}}$. This ratio of H1's P_{MAX} to H2's P_{MAX} continued to converge as H1 exhibited 108.58%, 106.18%, and 104.33% the maximum power of H2 at 20.0, 30.0, and 50.0 A$_{\text{rms}}$, respectively. In our 100.0 A$_{\text{rms}}$ simulation results of Table I, H1's P_{MAX} is merely 103.48% H2's P_{MAX}, further exhibiting the trend to convergence between the P_{MAX} of the hybrid designs.

To further emphasize the effects of material ordering on power harvest, two hybrid core designs of the same geometries and configurations as described in Table II were simulated at a very low $I_P = 0.5$ A $_{\text{rms}}$ and a very high $I_P = 500.0$ A$_{\text{rms}}$ primary current condition using our semianalytical model validated in Section V. The H1 model used magnetic material parameters of $\mu_{\text{eff1}} = 15\,000$, $B_{\text{SAT1}} = 2.0$ T, $\mu_{\text{eff2}} = 30\,000$, $B_{\text{SAT2}} = 1.2$T. The H2 model used magnetic material parameters of $\mu_{\text{eff1}} = 30\,000$, $B_{\text{SAT1}} = 1.2$T, $\mu_{\text{eff2}} = 15\,000$, $B_{\text{SAT2}} = 2.0$T. Fig. 10 overlays the simulated power harvest for each hybrid design at the 0.5 A$_{\text{rms}}$ primary current excitation. We see that H2, the hybrid design featuring a high μ_{eff} material as its *inner* core, outperforms H1 at this low current excitation, where coupling and thus high μ_{eff} in the shortest core flux path is critical to harvester performance.

Fig. 11 alternatively shows the near identical performance of the hybrid designs under a very large primary current excitation. These experimental and simulation results are consistent with the CTMEH magnetic material parameter intuition discussed in Section I of this article. At "low" currents, coupling, and thus high permeability, is essential. At "high" currents, high saturation flux density designs yield the best power harvest. The ordering of the core materials in a hybrid design, therefore, is a key consideration at low currents. Alternatively, the material ordering does not have a significant impact on power harvest performance as primary currents grow very large.

VII. CONCLUSION

This article derived a nonlinear power harvest model for hybrid magnetic energy harvesters. Detailed quantifications of the bounds of the saturating harvester power transfer window and the harvester magnetizing inductance current were expressed in terms of harvester design parameters and magnetic material parameters. The mathematical model was implemented in Python and validated against experimental data for two hybrid, multicore harvester designs constructed from different combinations of nanocrystalline and si-steel split toroids. According to experimental results, the ordering of inner and outer core materials in a hybrid design does have a noticeable effect of average power harvest, and this effect diminishes as primary current excitations increase. This work presents a theoretical framework within which we imagine designers can evaluate very unconventional hybrid core designs, including even those that may not be currently fabricable with contemporary manufacturing tools. Hybrid harvester designs exploring, for example, gradual magnetic material variations along a radial gradient or periodic stacks of magnetic materials could prove useful or interesting for certain CTMEH applications.

ACKNOWLEDGMENT

The authors would like to thank Khang Le for his valuable contributions to the magnetic core experimental rig.

REFERENCES

[1] P. Jokic and M. Magno, "Powering smart wearable systems with flexible solar energy harvesting," in *Proc. IEEE Int. Symp. Circuits Syst.*, 2017, pp. 1–4.
[2] Y. K. Tan and S. K. Panda, "Optimized wind energy harvesting system using resistance emulator and active rectifier for wireless sensor nodes," *IEEE Trans. Power Electron.*, vol. 26, no. 1, pp. 38–50, Jan. 2011.
[3] W. Xiu, Y. Yao, L. Li, X. Li, and J. Wu, "A novel piezoelectric-electromagnetic vibration energy harvesting device with real-time adjustable resonant frequency," *IEEE Access*, vol. 13, pp. 91215–91231, 2025.
[4] C. Quintáns, J. Marcos-Acevedo, and C. Martıńez-Peñalver, "Thermoelectric energy harvesting system based on water-stored energy and daily ambient temperature variations," *IEEE Sensors J.*, vol. 20, no. 23, pp. 13919–13929, Dec. 2020.
[5] S. Fang et al., "High output, lightweight and small-scale rotational piezoelectric energy harvester utilizing internal impact effect," *Energy Convers. Manage.*, vol. 322, 2024, Art. no. 119180. [Online]. Available: https://www.sciencedirect.com/science/article/pii/S019689042401121X

[6] X. Huang and B. Yang, "Improving energy harvesting from impulsive excitations by a nonlinear tunable bistable energy harvester," *Mech. Syst. Signal Process.*, vol. 158, 2021, Art. no. 107797. [Online]. Available: https://www.sciencedirect.com/science/article/pii/S0888327021001928

[7] X. H. Xiao Zhang and B. Wang, "A quad-stable nonlinear piezoelectric energy harvester with piecewise stiffness for broadband energy harvesting," *Nonlinear Dyn.*, vol. 112, pp. 19633–19652, 2024. [Online]. Available: https://link.springer.com/article/10.1007/s11071-024-10077-0

[8] D. Khan et al., "A high-efficient wireless power receiver for hybrid energy-harvesting sources," *IEEE Trans. Power Electron.*, vol. 36, no. 10, pp. 11148–11162, Oct. 2021.

[9] S. C. Chandrarathna, S.-Y. Moon, and J.-W. Lee, "A power management system for hybrid energy harvesting from multiple multitype sources and ultrawide range source tracking," *IEEE Trans. Power Electron.*, vol. 38, no. 4, pp. 4859–4875, Apr. 2023.

[10] T. Lu et al., "A thermoelectric energy harvesting system assisted by a piezoelectric transducer achieving 10-mv cold-startup and 82.7% peak efficiency," *IEEE Trans. Power Electron*, vol. 39, no. 5, pp. 6352–6363, May 2024.

[11] J. Moon and S. B. Leeb, "Analysis model for magnetic energy harvesters," *IEEE Trans. Power Electron.*, vol. 30, no. 8, pp. 4302–4311, Aug. 2015.

[12] D. Monagle, E. Ponce, and S. B. Leeb, "Generalized analysis method for magnetic energy harvesters," *IEEE Trans. Power Electron.*, vol. 37, no. 12, pp. 15764–15773, Dec. 2022.

[13] W. Zhou, Z. Liu, Q. Huang, Y. Jiang, and Z. Cong, "Design of magnetic cores for current transformer energy harvesting devices," in *Proc. 2019 IEEE PES Asia-Pacific Power Energy Eng. Conf.*, 2019, pp. 1–5.

[14] B. Park et al., "The magnetic energy harvester with improved power density using saturable magnetizing inductance model for maintenance applications near high voltage power line," *IEEE Access*, vol. 9, pp. 82661–82674, 2021.

[15] A. Abramovitz, M. Shvartsas, G. I. Orfanoudakis, and A. Kuperman, "Output characteristics of passive magnetic energy harvester feeding a constant-voltage-type load," *IEEE Trans. Emerg. Sel. Topics Power Electron.*, vol. 13, no. 3, pp. 2966–2974, Jun. 2025.

[16] J. Moon and S. B. Leeb, "Power electronic circuits for magnetic energy harvesters," *IEEE Trans. Power Electron.*, vol. 31, no. 1, pp. 270–279, Jan. 2016.

[17] M. Gao, L. Yi, and J. Moon, "Enabling multiple harvesting windows in magnetic energy harvesting via reverse flux desaturation," *IEEE Trans. Emerg. Sel. Topics Power Electron.*, vol. 12, no. 3, pp. 2517–2530, Jun. 2024.

[18] M. Gao, L. Yi, and J. Moon, "Intracycle gapless core desaturation via crisscross switches for maximal magnetic energy harvesting," *IEEE Trans. Ind. Electron.*, vol. 72, no. 3, pp. 2476–2486, Mar. 2025.

[19] Y. Zhuang et al., "Improving current transformer-based energy extraction from ac power lines by manipulating magnetic field," *IEEE Trans. Ind. Electron.*, vol. 67, no. 11, pp. 9471–9479, Nov. 2020.

[20] C. Xu, W. Wang, W. Su, M. Duan, and M. Hu, "Antisaturation and power decoupling control of multiwinding energy harvester based on magnetomotive force compensation," *IEEE Trans. Ind. Informat.*, vol. 19, no. 10, pp. 10555–10563, Oct. 2023.

[21] J. Wang, J. Kim, and D. S. Ha, "Powerline energy harvesting circuit with a desaturation controller for a magnetic core," in *Proc. 2021 IEEE Int. Midwest Symp. Circuits Syst.*, 2021, pp. 220–223.

[22] D. Monagle, E. Ponce, and S. B. Leeb, "Resonant circuits for split-core magnetic energy harvesters," *IEEE Trans. Ind. Electron.*, vol. 71, no. 8, pp. 9932–9941, Aug. 2024.

[23] M. Gao, L. Yi, and J. Moon, "Mathematical modeling and validation of saturating and clampable cascaded magnetics for magnetic energy harvesting," *IEEE Trans. Power Electron.*, vol. 38, no. 3, pp. 3455–3468, Mar. 2023.

[24] Z. Liu, Y. Li, Z. Hu, Z. Zang, X. Wen, and Z. He, "A wide-range self-powered current measurement method based on induced current multiplexing for online monitoring devices in transmission lines," *IEEE Trans. Circuits Syst. I: Reg. Papers*, vol. 72, no. 3, pp. 1486–1494, Mar. 2025.

[25] W. Wang, C. Xu, C. Zhang, and C. Chen, "Start-up and saturation optimization of high-power energy harvester with compound topologies overhead ac transmission line," *IEEE Trans. Emerg. Sel. Topics Power Electron.*, vol. 8, no. 4, pp. 3609–3617, Dec. 2020.

[26] S. Paul, S. Bashir, and J. Chang, "Design of a novel electromagnetic energy harvester with dual core for deicing device of transmission lines," *IEEE Trans. Magn.*, vol. 55, no. 2, Feb. 2019, Art. no. 8000104.

[27] D. Monagle and S. B. Leeb, "Nonlinear, hybrid, multi-core magnetic energy harvesting," *IEEE Trans. Power Electron.*, early access, Sep. 9, 2025, doi: 10.1109/TPEL.2025.3607641.

[28] A. Kuperman, "Optimal load type for passive magnetic energy harvesters," *IEEE Sens. Lett.*, vol. 9, no. 4, Apr. 2025, Art. no. 2501604.

[29] Nanocrystalline Silicon Steel (CRGO) Cut Core, Guangzhou Amorphous Electronic Technology Co., ltd., Accessed 2025, product page. [Online]. Available: https://www.coilcore.com/nanocrystalline-silicon-steel-crgo-cut-core_p10.html

[30] VITROPERM 800 / 500, Accessed 2025, product information. [Online]. Available: https://vacuumschmelze.com/03_Documents/Brochures/VITROPERM%20500%20-%20800.pdf

Daniel Monagle (Graduate Student Member, IEEE) received the B.S. and S.M. degrees in electrical engineering and computer science from the Massachusetts Institute of Technology, Cambridge, MA, USA, in 2020 and 2022, respectively, where he is currently working toward the Ph.D. degree in electrical engineering and computer science.

His research interests include energy harvesting, magnetics, low-power circuit design, and self-powered systems.

Mr. Monagle was the recipient of the MIT School of Engineering 2023–2024 Thomas G. Stockham Jr. Fellowship for excellence in teaching and mentoring, and the IEEE Sensors Journal 2025 Best Paper Award.

Steven B. Leeb (Fellow, IEEE) received the Ph.D. degree from the Massachusetts Institute of Technology, Cambridge, MA, USA, in 1993.

He was a Commissioned Officer with the USAF Reserve, Robins Air Force Base, GA, USA. Since 1993, he has been a Member of the MIT Faculty with the Department of Electrical Engineering and Computer Science. He also holds a joint appointment with MIT's Department of Mechanical Engineering. He has authored or coauthored more than 200 publications and 20 U.S. Patents in the fields of electromechanics and power electronics.